J. Phys.: Condens. Matter 7 (1995) 9357–9368. Printed in the UK

X-ray absorption spectroscopy study of $Ni_cMg_{1-c}O$ solid solutions on the Ni K edge

A Kuzmin†, N Mironova‡, J Purans† and A Rodionov†

† Institute of Solid State Physics, University of Latvia, LV-1063 Riga, Latvia

‡ Nuclear Research Centre, Latvian Academy of Science, LV-2169 Salaspils, Latvia

Received 21 April 1995, in final form 12 October 1995

Abstract. We present an x-ray absorption spectroscopy study of $Ni_cMg_{1-c}O$ ($0.01 \leqslant c \leqslant 1$) solid solutions on the Ni K edge. The analysis of XANES and EXAFS regions allowed us to obtain the following results. The nickel ions are located in a distorted environment and shift upon dilution to the off-centre positions. In the first shell, the average Ni–O distance increases linearly upon dilution. In the second shell, the average Ni–Ni distance remains unchanged and decreases slightly at low nickel concentration while the dependence of the average Ni–Mg distance has a break at $c \simeq 0.6$ and is nearly constant below and above this concentration which corresponds to the point of antiferromagnetic–paramagnetic phase transition. The number of nickel and magnesium ions in the second shell of nickel ions varies in agreement with the random distribution model. The results obtained are discussed in comparison with the ones from x-ray diffraction, optical spectroscopy and magnetic measurements.

1. Introduction

The $Ni_cMg_{1-c}O$ system forms a continuous series of solid solutions and at any composition has a rock-salt crystal structure in which metal ions occupy sites on a face-centred-cubic (fcc) lattice [1,2]. The lattice constant a depends, according to the x-ray diffraction (XRD) data [2], linearly on the composition: it increases slightly upon dilution from 4.1795 Å in pure NiO ($c = 1$) to 4.2113 Å in pure MgO ($c = 0$). Thus, since NiO is a type-II antiferromagnet with the Néel temperature $T_N = 523$ K [3] and MgO is a diamagnet, the $Ni_cMg_{1-c}O$ system is ideal for studying the effects of magnetic dilution on the magnetic properties.

The nature of magnetic ordering in $Ni_cMg_{1-c}O$ depends on the relative signs and strengths of the nearest-neighbour (NN) and next-nearest-neighbour (NNN) superexchange interactions between two Ni^{2+} ions via an oxygen ion [4, 5]. The NN interactions, having ferromagnetic and antiferromagnetic character, occur within three-atom chains Ni^{2+}–O^{2-}–Ni^{2+} with $\widehat{NiONi} = 90°$ (the so-called 90° pairs) and are characterized by the exchange parameter J_{NN}. The NNN interactions, having antiferromagnetic character, occur within linear three-atom chains Ni^{2+}–O^{2-}–Ni^{2+} with $\widehat{NiONi} = 180°$ (the so-called 180° pairs) and are characterized by the exchange parameter J_{NNN}. Since the variation of the crystal lattice constant a in $Ni_cMg_{1-c}O$ is small enough (about 0.7% [2]), one can expect that upon dilution the corresponding changes in J_{NN} and J_{NNN} should be negligible. Therefore, one can take it that the exchange parameters have the same values in solid solutions as in pure NiO: $J_{NN} \simeq 34$ K and $J_{NNN} \simeq 202$ K [5] (we use the positive and negative signs of J for antiferromagnetic and ferromagnetic interactions, respectively). A large difference between

0953-8984/95/489357+12$19.50

the two values of the exchange parameters means that a very different magnetic behaviour can be expected (and is observed) upon dilution in $Ni_cMg_{1-c}O$ [1, 2, 6].

A magnetic phase diagram of $Ni_cMg_{1-c}O$ solid solutions has been determined recently using elastic magnetic neutron scattering and SQUID magnetometry [2, 6]. There, four ranges have been defined [6]: (1) a homogeneous antiferromagnet ($0.63 \leqslant c \leqslant 1$); (2) a tricritical region or a frustrated antiferromagnet ($0.4 \leqslant c < 0.63$); (3) a spin-glass state ($0.25 \leqslant c < 0.4$); and (4) a diamagnet ($c \leqslant 0.2$). In the first region, a topologically infinite cluster diluted by diamagnetic Mg^{2+} ions occurs [2, 6] and the antiferromagnetic domain structure is observed up to certain temperatures [7]. At $c = 0.63$, the infinite cluster becomes destroyed; however, the type-II antiferromagnetism is still maintained upon dilution until $c = 0.4$ [6] ($c = 0.31$ [2]). Note that in these two regions only NNN exchange interactions play an important role and the long-range magnetic order is present [2, 6]. Below $c = 0.4$ [6] ($c = 0.31$ [2]), the NN exchange interactions become significant compared to the NNNs and a transition from long-range order (LRO) to short-range order (SRO) that occurs with the SRO phase appears to be a spin-glass-like state. For $c \leqslant 0.2$ [6] ($c < 0.15$ [2]), the system becomes paramagnetic: there are only the single Ni^{2+} ions and the exchange-coupled Ni^{2+} pairs which disappear for $c < 0.01$ [1, 8].

Thus the destruction in $Ni_cMg_{1-c}O$ of the magnetic LRO as a result of diamagnetic dilution is now well established. However, there is a lack of detailed structural data on the variation of the SRO around Ni^{2+} ions, since the previous XRD studies [1, 2] gave information only on the average lattice constant. Therefore it is of great interest to compare the SRO structural parameters with the LRO magnetic and structural information. Among existing tools, a unique method for probing the local environment around a specific atom is x-ray absorption spectroscopy [9]: it is sensitive to variations of the local electronic and atomic structures related mainly to site symmetry, interatomic distances, coordination numbers, thermal vibrations and static disorder.

In this work we report an x-ray absorption spectroscopy study of the $Ni_cMg_{1-c}O$ solid solutions on the Ni K edge. We have obtained information on the first and second coordination shells of nickel ions and compared it with the results from other techniques.

The paper is organized as follows: in section 2, the experimental procedures for the sample preparation and the x-ray absorption measurements are presented; in section 3, the data treatment procedure is described in detail; in section 4, we discuss our results and compare them with the results obtained by other techniques; in section 5, a summary of the present work and the main conclusions are given.

2. Experimental procedure

The samples of $Ni_cMg_{1-c}O$ ($c = 0.10$, 0.20, 0.35, 0.45, 0.50, 0.60, 0.70, 0.80 and 0.90) were prepared using the procedure of [1, 2] which is briefly described below. The amounts of aqueous solutions of $Mg(NO_3)_2{\cdot}6H_2O$ and $Ni(NO_3)_2{\cdot}6H_2O$ salts corresponding to the appropriate solid solution composition were mixed and slowly evaporated. The remaining dry 'flakes' were heated up to 500–600 °C to remove NO_2 completely. The polycrystalline solid solution obtained was powdered and annealed for 100 h at 1200 °C in air and then quickly cooled down to the room temperature. The compositions of the solid solutions were confirmed by instrumental neutron-activated analysis [1]. X-ray structural and phase analyses were carried out to control the prepared samples. It was found that the solid solutions were single phase and had rock-salt structure with a lattice constant depending linearly on the composition and being in good agreement with known data [1, 2].

Experimental x-ray absorption spectra at the Ni K edge in $Ni_cMg_{1-c}O$ solid solutions and pure NiO ($c = 1$) were measured in the transmission mode at the ADONE storage ring (Frascati, Italy) on the PWA-BX2S wiggler beam line. The storage ring ADONE operated at the average energy 1.2 GeV and with maximum stored current of 40 mA. A standard transmission scheme with a Si(220) channel-cut crystal monochromator and two ion chambers containing krypton gas was used. The experimental spectra were recorded at room temperature in the energy range from 8230 to 9300 eV. The samples were prepared from finely ground $Ni_cMg_{1-c}O$ powders and had a thickness leading to the absorption jump $\Delta\mu x$ of about 0.6–1.8 depending on the composition.

3. Data analysis

The x-ray absorption spectra were treated using the EDA software package following the standard procedure [10].

The E_0-position, defining the zero wavevector ($k = 0$), was set at the energy $E_0 = 8343$ eV. This energy point was found by the alignment of the experimental and calculated extended x-ray absorption fine-structure (EXAFS) signals for pure NiO. Such a choice of the E_0-position corresponds also to the maximum of the first derivative of the absorption coefficient for pure NiO. The E_0-value was fixed for all spectra at the same energy; therefore it was not affected by the strong variation of the fine structure at the absorption edge for small c (figure 1).

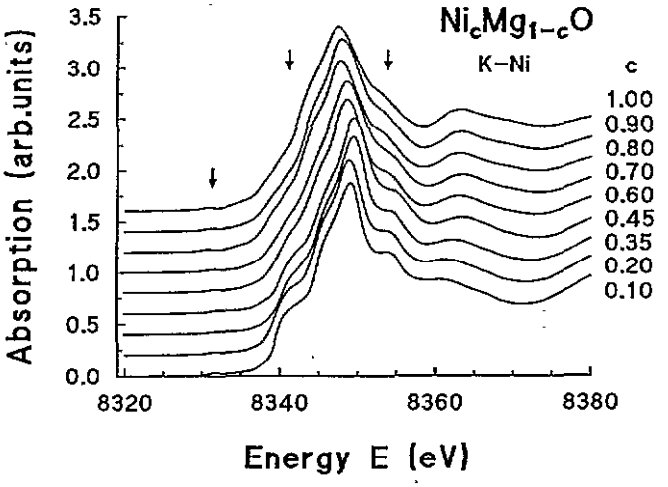

Figure 1. Normalized XANES spectra $\mu(E)$ at the Ni K edge in $Ni_cMg_{1-c}O$. The first arrow at ~8332 eV indicates the pre-edge peak related to the 1s(Ni) → 3d(Ni) + 2p(O) transition. Two other arrows at ~8340 and ~8354 eV show the energy ranges where strong variation of the XANES with the composition takes place.

The extracted experimental EXAFS spectra $\chi(k)k^2$ and their Fourier transforms (FT) are shown in figure 2. The FTs were calculated in the range from 1.0 to 14.0 $Å^{-1}$ with a Kaiser–Bessel window which gives results similar to the usual 10% Gaussian window but was found to be slightly more accurate [10]. Note that since FTs were calculated

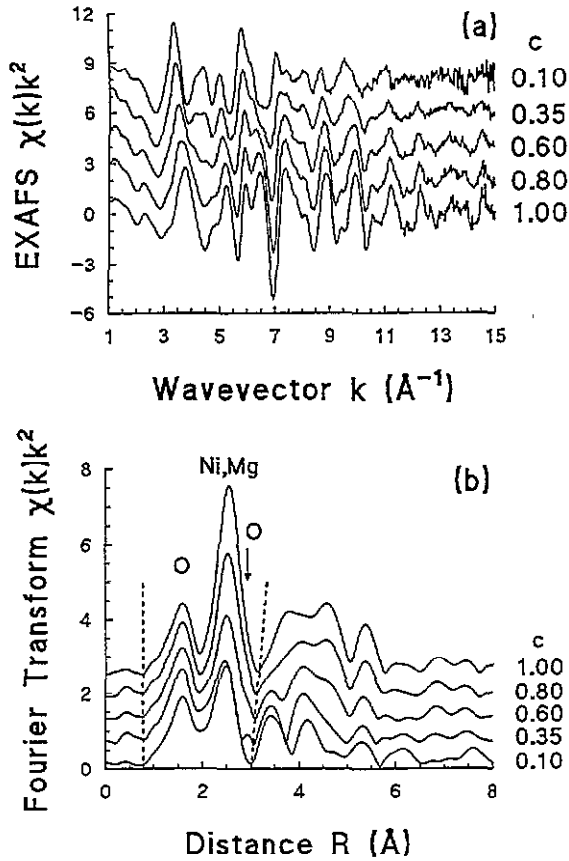

Figure 2. (a) Experimental EXAFS $\chi(k)k^2$-spectra in $Ni_cMg_{1-c}O$. (b) Fourier transforms of the spectra shown in (a). Dashed lines indicate the range used in the analysis.

without phase correction, the positions of the peaks in figure 2(b) differ from their true crystallographic values.

The exchange for nickel ions of magnesium ones leads to significant modifications of the peaks beyond the first one (figure 2(b)). The first peak at ~1.5 Å is related to the first shell composed of six oxygen atoms. The second peak at ~2.5 Å is mainly due to twelve atoms of the second shell which consists, depending on the composition of the solid solution, of either nickel atoms or nickel and magnesium atoms. However, there is an additional contribution due to eight oxygen atoms located in the third shell. These contributions are generally weak but not negligible and appear as a small shoulder on the right-hand side of the second peak (figure 2(b)). In k-space they produce rapidly damped oscillating signals giving the origin for the 'bump' at 2.0–2.5 $Å^{-1}$ (figure 3). The peaks beyond the second one (figure 2(b)) are due to the outer shells composed of nickel, magnesium and oxygen atoms. Their EXAFS signals are strongly overlapped in R-space and are highly influenced by the multiple-scattering effects due to a number of linear atom chains in the structure. As a result, the analysis of this region is complicated and is beyond the scope of this paper.

The EXAFS signals from the first two peaks were only used in the analysis (figure 3). They were singled out by the Fourier filtering procedure in the range shown in figure 2(b) by two dashed lines. These EXAFS signals were fitted using a multi-shell model:

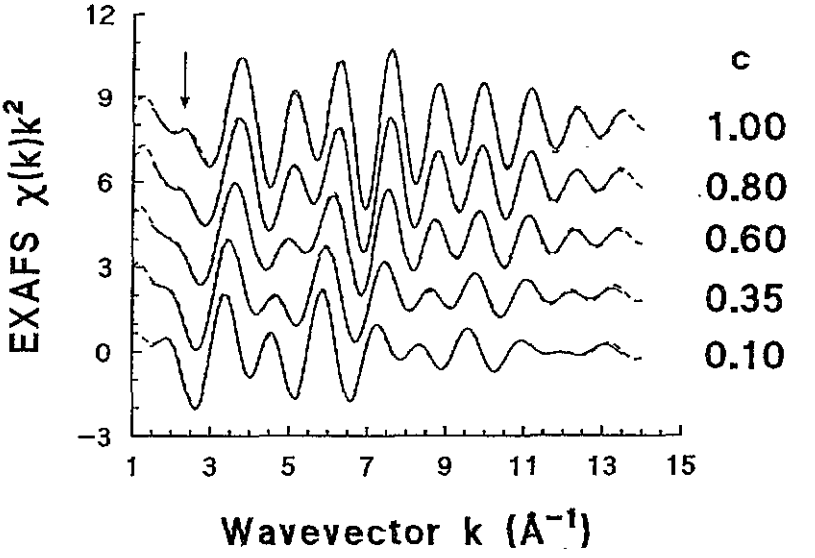

Figure 3. The best fit (solid lines) of the experimental (dashed lines) EXAFS $\chi(k)k^2$-spectra related to the range between two dashed lines in figure 2(b). Only a few spectra are shown for clarity. The arrow at ~2.5 $Å^{-1}$ indicates the feature whose origin is due to eight oxygen atoms located in the third shell and to the multiple-scattering effects in the first shell.

$$\chi(k) = \sum_{i=1}^{m} (N_i/kR_i^2) f_i(\pi, k, R_i) \exp(-2\sigma_i^2 k^2) \sin(2kR_i + \phi_i(\pi, k, R_i)). \quad (1)$$

Here $k = \sqrt{(2m_e/\hbar^2)(E - E_0 - \Delta E_{0i})}$ is the photoelectron wavevector; ΔE_{0i} the E_0 correction; N_i the coordination number; R_i the interatomic distance; and σ_i^2 the Debye–Waller (DW) factor describing both static and thermal disorder. $f_i(\pi, k, R_i)$ is the back-scattering amplitude of the photoelectron, and $\phi_i(\pi, k, R_i)$ is the total phase shift function of the photoelectron due to the neighbour and absorber atoms. They were calculated using the FEFF3 code [11] for Ni–O_1 ($R = 2.095$ Å), Ni–Ni_2 ($R = 2.965$ Å), Ni–Mg_2 ($R = 2.965$ Å) and Ni–O_3 ($R = 3.63$ Å) pairs. The muffin-tin radii were chosen according to the Norman criterion [12] and were reduced by a factor 0.85. They were equal to 1.14 Å for the absorber (Ni) and 0.94 Å (O), 1.16 Å (Ni) and 1.37 Å (Mg) for the neighbouring atoms. The complex Hedin–Lundqvist potential [13] was used to describe the exchange and correlation effects; therefore $f_i(\pi, k, R_i)$ automatically included the correction on the mean free path. Natural broadening was included through the core-level width $\Gamma_{\text{core-hole}}$(K–Ni) = 1.6 eV [14].

The number m of components, related to the EXAFS signals which contribute into the first two peaks in the FT (figure 2(b)), was equal to three or four depending on the composition of the solid solution. Three components were used in the fits of the EXAFS signals for pure NiO ($c = 1$). In this case, the three components correspond, respectively, to oxygen atoms of the first shell, nickel atoms of the second shell and oxygen atoms of the third shell. In the solid solutions with $c \leqslant 0.8$ four components were necessary to describe the experimental EXAFS signals. These components were due to oxygen atoms of the first shell, nickel and magnesium atoms of the second shell and oxygen atoms of the third shell. The fit of the solid solution with $c = 0.90$ was performed using three and four components: it was found that the three-component fit, taking into account only the nickel atoms in the second shell, gives significantly better agreement with the experimental EXAFS signal.

Thus we used up to 16 fitting parameters (four (N_i, R_i, σ_i^2, ΔE_{0i}) for each shell) which is fewer than the number of independent data points $N_{\text{ind}} \simeq 20$ ($N_{\text{ind}} = 2\Delta k \Delta R/\pi + 2$ where Δk and ΔR are respectively the widths in k- and R-space used in the fit [15]). The inclusion of the ΔE_{0i} fitting parameters was for two reasons: (1) to compensate for the relative difference of the energy origins in the theoretical amplitude and phase functions $f_i(\pi, k, R_i)$ and $\phi_i(\pi, k, R_i)$ calculated for the different atom pairs; and (2) to compensate for the absolute shift of the E_0-position within the series of solid solutions due to modifications of the local electronic structure around nickel ions under transition from the crystal-like state in pure NiO to the impurity-like state at low concentrations. The values of ΔE_{0i} were found to be nearly constant (the variations of their values for different EXAFS spectra were less than 2 eV) and equal to 3.5, 4.5 and 6.0 eV for the first (Ni–O_1), the second (Ni–Ni_2 and Ni–Mg_2) and the third (Ni–O_3) shells, respectively.

Table 1. Structural data obtained from the best-fit analysis of the Ni K-edge EXAFS in $Ni_cMg_{1-c}O$. (N (±0.5) is the number of atoms A_i located in the i-shell (i = 1, 2, 3) at distance R (±0.005 Å) from the nickel; σ^2 is the Debye–Waller factor (±0.0007 Å^2); ε is the fitting error calculated using equation (2).)

		c								
A_i		1.0	0.90	0.80	0.70	0.60	0.45	0.35	0.20	0.10
	N	5.9	6.2	6.3	6.3	6.2	5.6	6.2	6.0	5.2
O_1	R	2.089	2.088	2.089	2.094	2.095	2.098	2.098	2.100	2.106
	σ^2	0.0038	0.0040	0.0042	0.0043	0.0043	0.0033	0.0042	0.0039	0.0028
	N	11.5	10.3	9.5	7.5	6.3	3.9	3.8	2.1	1.0
Ni_2	R	2.956	2.957	2.957	2.957	2.956	2.952	2.952	2.948	2.946
	σ^2	0.0054	0.0054	0.0055	0.0050	0.0050	0.0040	0.0045	0.0039	0.0024
	N			2.3	4.1	4.4	7.2	8.1	9.7	10.8
Mg_2	R			2.961	2.958	2.961	2.973	2.976	2.977	2.980
	σ^2			0.0034	0.0040	0.0041	0.0037	0.0038	0.0042	0.0046
	N	5.8	7.2	7.4	8.6	9.8	17.3	15.5	18.8	23.0
O_3	R	3.51	3.52	3.51	3.51	3.54	3.57	3.59	3.60	3.61
	σ^2	0.009	0.007	0.012	0.013	0.021	0.048	0.029	0.034	0.035
	ε ($\times 10^{-3}$)	4.2	3.3	2.6	2.6	3.3	5.0	3.3	4.5	3.3

The calculated EXAFS signals were in good agreement with the experimental ones at all compositions (figure 3). The fitting error was calculated using the expression [10]

$$\varepsilon = \frac{1}{n}\sum_{i=1}^{n}(\chi_{\text{model}}(k_i)k_i^2 - \chi_{\text{experiment}}(k_i)k_i^2)^2 \qquad (2)$$

where n is the number of data points. The values of structural parameters obtained are presented in table 1 and their dependences versus c are shown in figures 4 and 5. Note that the neglect by the EXAFS contribution of the third-shell oxygen atoms does not affect the values of the structural parameters for the first and the second shells; however, the fitting error increases and the 'bump' in the EXAFS signals at 2.0–2.5 Å^{-1} (figure 3) cannot be reproduced.

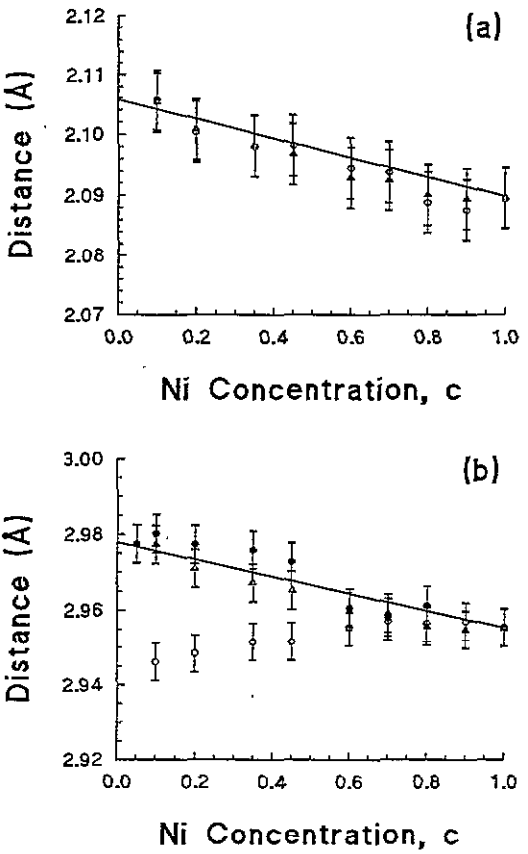

Figure 4. The variation of the interatomic distances R(Ni–O) (a), R(Ni–Ni) (open circles) and R(Ni–Mg) (solid circles) (b) with the composition in $Ni_cMg_{1-c}O$. Their values calculated in the VCA from the average crystal lattice parameter, obtained from XRD [1, 2] (solid line) and EXAFS (triangles) data, are also shown.

4. Results and discussion

The x-ray absorption near-edge structures (XANES) of $Ni_cMg_{1-c}O$ are shown in figure 1. They are similar in all solid solutions except that some features become more pronounced upon dilution. Small shifts in the energy position of the features are also observed.

Interpretation of the XANES in pure NiO has been made recently using the multiple-scattering approach [16]. It was found that the features observed in the experiment (figure 1) are due to the scattering effects within about nine shell clusters of 6.6 Å radius [16]. The interpretation of XANES in solid solutions is analogous [17]: here the visible differences are only caused by the change of the lattice constant with the composition and by the differences in the scattering amplitude and phase shift functions of nickel and magnesium atoms. The first effect is responsible for the shift in the energy position of the features while the second one is responsible for the modifications of their shapes. The interpretation of the observed effects in terms of the densities of states can be done using the results of the *ab initio* periodic unrestricted Hartree–Fock calculations [18]. They show that the differences in the densities of states as functions of concentration c are due to the changes in the intersite hybridization of nickel and oxygen orbitals. The widths of the Ni bands

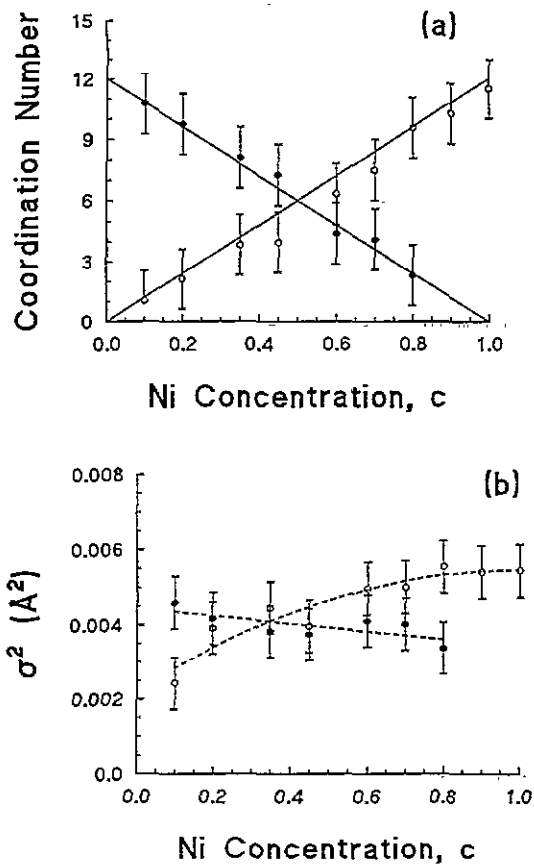

Figure 5. The variation of the number of nickel and magnesium ions (a) and the Debye–Waller factors for the Ni–Ni (open circles) and Ni–Mg (solid circles) atom pairs (b) in the second shell with the composition. Solid lines in (a) correspond to the expected number of nickel and magnesium ions in accordance with the formal composition. The dashed lines in (b) are guides for the eye.

at different values of c are determined by the number of superexchange interactions via oxygen with smaller contributions from direct nickel–nickel overlap; therefore the widths increase slightly with the increase of the number of nickel neighbours [18] leading to the broadening of the XANES features at high concentrations (figure 1).

In pure NiO the pre-edge peak appears at 8332 eV (figure 1) [19]. Its origin is due to the $1s(Ni) \rightarrow 3d(Ni) + 2p(O)$ transition which is forbidden in the dipole approximation for a perfect NiO_6 octahedron but becomes allowed when the inversion centre is absent or a strong mixing of the oxygen p and nickel d states occurs [19, 20]. Note that a similar pre-edge peak exists also in solid solutions.

The earlier observations in the optical absorption and luminescence spectra of the $Ni_cMg_{1-c}O$ monocrystals [21] show evidence of the distortion of the local environment around nickel ions. The optical absorption spectra in the energy range 7800–8300 cm^{-1} correspond to $^3A_{2g} \rightarrow {}^3T_{2g}$ magneto-dipole transitions at Ni^{2+} sites and consist of two absorption lines at 8005 and 8182 cm^{-1} [21]. We believe that these lines are due to the splitting of $^3T_{2g}$ excited states by a crystal field acting on nickel ions located at the off-centre

positions [22]. The same splitting occurs in the luminescence spectra [21]. Moreover the additional lines, appearing in this energy range at the nickel concentration $c > 0.01$ and related to the zero-phonon electron transitions, support the presence of the exchange-coupled pairs (the so-called 90° pairs) of Ni^{2+} ions [1, 21].

The results of the EXAFS spectra analysis are presented in table 1. Good agreement was found for the structural data (distances and coordination numbers) for pure NiO in the first and the second shells (Ni–O_I and Ni–Ni_2) compared to the ones obtained by XRD [1, 2]. However, the data for the third oxygen shell differ from the XRD results: the Ni–O_3 distance (3.51 Å), determined by EXAFS, is shorter by ~0.11 Å than the one (3.62 Å) calculated from the lattice parameter, and the number of oxygen atoms in the third shell is smaller than the crystallographic value (eight oxygen atoms). Upon dilution, the difference between the values of the Ni–O_3 distance given by EXAFS and XRD decreases while the difference between the values of the coordination number increases rapidly (table 1). Such behaviour occurs mainly for two reasons: (1) a strong correlation between the coordination number and the DW factor due to the contribution of the EXAFS signal from the third shell is small enough; and (2) the presence of two multiple-scattering signals, generated within Ni–O_I^I–O_I^{II}–Ni ($\widehat{O_I^I Ni O_I^{II}} = 90°$) and Ni–$O_1$–Ni$(Mg)_2$–Ni ($\widehat{NiO_1 Ni(Mg)_2} = 90°$) atom chains (here O_I^I and O_I^{II} denote two different oxygen atoms located in the first shell), which contribute in the same FT range as the third-shell EXAFS signal leading to its distortion. Therefore, for the above reasons, we excluded the structural data obtained for the third shell from the following analysis.

The coordination number $N_1 = 6.0 \pm 0.5$ and the DW factor $\sigma_1^2 = 0.0038 \pm 0.0007$ Å^2, related to oxygen atoms of the first shell, remain constant upon dilution within the error bar of the experiment. The variations of other structural parameters versus c are shown in figures 4 and 5. Note that the change in the number of nickel and magnesium ions in the second shell (figure 5(a)) correlates well with the random distribution model.

The variation of the lattice parameter $a(c)$ in $Ni_cMg_{1-c}O$, determined by XRD [1, 2], is linear. It can be interpreted using Vegard's law [1] or the *virtual-crystal approximation* (VCA) [23]. Vegard's law states that the lattice parameter of the solid solution is equal to the additive sum of the lattice parameters of individual components weighted by the concentrations of each of the parts. In this model, the values of the bond lengths Ni–O and Mg–O are considered to be constant as in NiO and MgO. In the VCA, it is assumed that the atoms are located on the ideal lattice sites of the average unit cell, and average values for bond lengths, bond ionicity, atomic potentials, etc are considered. Therefore, in the framework of the VCA, the Ni–O and Ni–Ni (Ni–Mg) distances obey the rules $R(c) = a(c)/2$ and $R(c) = a(c)\sqrt{2}/2$, respectively, i.e. they vary as the lattice parameter $a(c)$ does.

The EXAFS analysis shows that the Ni–O distance varies linearly upon dilution (figure 4(a)) in agreement with the VCA. In contrast, the variations of the Ni–Ni and Ni–Mg distances differ strongly from the ones expected in the VCA (figure 4(b)). The dependence of the Ni–Mg distance on the composition has a break at $c \simeq 0.6$ and is nearly constant below and above this concentration. The values of the Ni–Mg distance are higher than the ones expected in the VCA for $c < 0.6$ and comparable to them for $c > 0.6$. The Ni–Ni distance is almost constant for $c > 0.6$ and slightly decreases upon dilution. The values of the Ni–Ni distance are close to the ones expected from Vegard's law but are always smaller than the ones expected in the VCA. These results can be explained by strong NN interactions of nickel ions [2, 6] due to the fact that upon dilution they tend to shift from the centre of the oxygen octahedron. This process leads at low nickel concentration to formation of Ni–Ni coupled pairs [6, 24]. The ionic radii of Mg^{2+} and Ni^{2+} ions, which

are, respectively, 0.79 and 0.77 Å (taking, according to Goldschmidt [25], the radius of an oxygen ion equal to 1.32 Å), are also favourable to such a shift: the lattice constant increases upon dilution and nickel ions, having smaller size than magnesium ones, become more mobile.

To understand why the EXAFS results, unlike the XRD results, do not completely follow Vegard's law or the VCA, one should remember that the lattice parameter $a(c)$ is calculated from the diffraction pattern given by different crystallographic planes. Therefore, the value of $a(c)$ is averaged over all crystallographic directions and, thus, one should compare it with the analogous quantity given by EXAFS. From the distances obtained up to the first and second shells, we calculated the average lattice parameter determined from EXAFS data as

$$a_{\mathrm{EXAFS}} = [2R(\mathrm{Ni\text{–}O}) + 2(cR(\mathrm{Ni\text{–}Ni}) + (1-c)R(\mathrm{Ni\text{–}Mg}))\cos(45°)]/2 \quad (3)$$

where the first term in the square brackets corresponds to the lattice constant along the ⟨100⟩ directions and the second term corresponds to the lattice constant along the ⟨110⟩ directions. It is interesting to note that although the Ni–Ni and Ni–Mg distances do not obey the VCA, the average lattice parameter obtained from EXAFS data agrees well with the one calculated from XRD data [1, 2] (see the triangles and solid lines in figure 4).

The behaviour of the Ni–Ni and Ni–Mg interatomic distances correlates with the variation of the DW factors for Ni–Ni and Ni–Mg atom pairs (figure 5(b)). At high nickel concentration $c > 0.35$, the Ni–Ni DW factor dominates over the Ni–Mg one since the magnesium ions, having larger size, are squeezed in the NiO lattice. At low nickel concentration $c < 0.35$, the Ni–Mg DW factor dominates over the Ni–Ni one since it increases due to the static disorder caused by the off-centre position of nickel ions, while the Ni–Ni DW factor decreases owing to the strong NN exchange interaction. Apparently, the cross point of the DW factor dependences at $c \simeq 0.35$ correlates with the experimental percolation threshold $c_{\mathrm{perc}} \simeq 0.31$ below which the NN exchange interaction becomes important compared to the NNN one [2]. Note also that the decrease of the Ni–Ni distance occurs below that concentration (figure 4(b)). However, the solution of this requires further more accurate investigation.

Now we compare the results obtained with the magnetic phase diagram [6], described in section 1. Since all the EXAFS measurements were performed at room temperature, one should look at the cut of the diagram along the line $T \simeq 300$ K. There two special points exist upon dilution [6]: at $c = 0.8$, the destruction of the infinite antiferromagnetic domain structure is observed—however, the solid solution remains antiferromagnetic; while at $c = 0.6$, the value of the Néel temperature T_N crosses room temperature and the transition from an antiferromagnetic to a paramagnetic phase occurs. The EXAFS results show that above $c = 0.6$ the distances Ni–Mg and Ni–Ni are nearly the same, but for $c < 0.6$ the difference between them increases rapidly (figure 4(b)). This correlates well with the neutron diffraction data: it was found [6] that the (1/2 1/2 1/2) magnetic peak has no detectable broadening above $c = 0.6$ and its width increases rapidly below this concentration which can be explained by the presence of two different distances within the metal sublattice for $c < 0.6$ (figure 4(b)).

5. Summary and conclusions

In this work we carried out an x-ray absorption spectroscopy study of $Ni_cMg_{1-c}O$ ($0.01 \leqslant c \leqslant 1$) solid solutions on the Ni K edge.

We found that unlike the lattice parameter obtained by XRD [1, 2], the interatomic distances given by EXAFS do not completely follow either Vegard's law or the virtual-crystal approximation (VCA). However, the average lattice parameter obtained from EXAFS data for the first and the second shells agrees well with the one calculated from XRD data [1, 2]. Deviation of the bond length composition dependence from that given by Vegard's law or the VCA model has also been observed in some binary substitutional alloys [26, 27].

In more detail, the results of the EXAFS analysis are as follows.

The average Ni–O distance increases linearly upon dilution in agreement with the VCA, and the number of nickel and magnesium ions in the second coordination shell of nickel varies in agreement with the random distribution model.

Nickel ions are located in the distorted local environment and shift upon dilution to the off-centre positions. The nickel displacements occur due to the NN exchange interactions between any of two Ni^{2+} ions and are favoured by the increase of the lattice parameter at small c-values. The average Ni–Ni distance remains unchanged for $c > 0.6$ and decreases slightly for low nickel concentration. The observed off-centre position of nickel ions is also supported by the Debye–Waller factor variations and by the presence of the pre-edge peak in the Ni K-edge XANES. It is also in good agreement with the results of the optical absorption and luminescence measurements [21].

The dependence of the average Ni–Mg distance on the composition has a break at $c \simeq 0.6$ and is nearly constant below and above this concentration, which corresponds to the point of the transition from an antiferromagnetic to a paramagnetic phase.

Acknowledgments

JP is grateful to Professor E Burattini (Laboratori Nazionali di Frascati) and to the staff of the PWA laboratory for making it possible to make measurements at the PWA-BX2S beam line. This work was supported in part by the International Science Foundation, grants LF8000 and LJ8100.

References

[1] Mironova N A and Ulmanis U A 1988 *Radiation Defects and Metal Ions of the Iron Group in Oxides* (Riga: Zinatne) (in Russian)
[2] Feng Z and Seehra M S 1992 *Phys. Rev.* B **45** 2184
[3] Roth W L 1958 *Phys. Rev.* **110** 1333
[4] ter Haar D and Lines M E 1962 *Phil. Trans. R. Soc.* A **254** 521
Seehra M S and Giebultowicz T M 1988 *Phys. Rev.* B **38** 11 898
[5] Towler M D, Allan N L, Harrison N M, Saunders V R, Mackrodt W C and Aprà E 1994 *Phys. Rev.* B **50** 5041
[6] Menshikov A Z, Dorofeev Yu A, Klimenko A G and Mironova N A 1991 *Phys. Status Solidi* b **164** 275; 1990 *Pis. Zh. Eksp. Teor. Fiz.* **51** 640
[7] Mironova N A, Belyaev A T, Miloslavskaya O V and Bandurkina G V 1981 *Ukr. Fiz. Zh.* **26** 848
[8] Archipov A A 1981 *Izv. Akad. Nauk Latvian SSR, Ser. Fiz. Tech. Nauk.* **3** 24
[9] Wong J 1986 *Mater. Sci. Eng.* **80** 107
[10] Kuzmin A 1995 *Physica* B **208+209** 175; 1993 *EDA: EXAFS Data Analysis Software Package. User's Manual* (private communication)
Rocca F, Kuzmin A, Purans J and Mariotto G 1994 *Phys. Rev.* B **50** 6662
[11] Rehr J J, Mustre de Leon J, Zabinsky S I and Albers R C 1991 *J. Am. Chem. Soc.* **113** 5135
Mustre de Leon J, Rehr J J, Zabinsky S I and Albers R C 1991 *Phys. Rev.* B **44** 4146
[12] Norman J G 1974 *Mol. Phys.* **81** 1191

[13] Hedin L and Lundqvist B I 1971 *J. Phys. C: Solid State Phys.* 4 2064
[14] Keski-Rahkonen O and Krause M O 1974 *At. Data Nucl. Data Tables* **14** 139
[15] Stern E A 1993 *Phys. Rev.* B **48** 9825
[16] Kizler P 1992 *Phys. Rev.* B **46** 10 540
[17] Sánchez del Río M 1991 private communication
[18] Towler M D, Allan N L, Harrison N M, Saunders V R and Mackrodt W C 1995 *J. Phys.: Condens. Matter* **7** 6231
[19] Asakura K, Iwasawa Y and Kuroda H 1986 *J. Physique Coll.* **47** C8 317
[20] Kuzmin A, Mironova N, Purans J and Sazonov A 1993 *Phys. Status Solidi* a **135** 133
Kuzmin A and Purans J 1993 *J. Phys.: Condens. Matter* **5** 9423
[21] Mironova N A, Grinvald G A, Skvorcova V N and Ulmanis U A 1981 *Fiz. Tverd. Tela* **23** 1498
Grinvald G A and Mironova N A 1983 *Izv. Akad. Nauk Latvian SSR, Ser. Fiz. Tech. Nauk* **1** 22, 28
[22] Mironova N A, Kuzmin A, Purans J and Rodionov A 1995 *Proc. SPIE* at press
[23] Letardi A, Motta N and Balzarotti A 1987 *J. Phys. C: Solid State Phys.* **20** 2853
[24] Chudinova S A, Kuz'kina S L and Shivrin O N 1969 *Fiz. Tverd. Tela* **11** 2375
[25] Goldschmidt V M 1927 *Berichte* **60** 1263
[26] Renaud G, Motta N, Lançon and Belakhovsky M 1988 *Phys. Rev.* B **38** 5944
[27] Thornton J M C, Unsworth P, Newell M A, Weightman P, Jones C, Bilsborrow R and Norman D 1994 *Europhys. Lett.* **26** 259